Bouncing window for colliding nanoparticles: Role of dislocation generation

Maureen L. Nietiadi,[1] Emmanuel N. Millán,[2] Eduardo M. Bringa,[3] and Herbert M. Urbassek[1,*]

[1]*Fachbereich Physik und Forschungszentrum OPTIMAS, Universität Kaiserslautern, Erwin-Schrödinger-Straße, D-67663 Kaiserslautern, Germany*

[2]*CONICET and Facultad de Ciencias Exactas y Naturales, Universidad Nacional de Cuyo, Mendoza 5500, Argentina*

[3]*CONICET and Facultad de Ingenería, Universidad de Mendoza, Mendoza 5500, Argentina*

(Received 10 November 2018; revised manuscript received 1 February 2019; published 21 March 2019)

Available macroscopic theories—such as the Johnson-Kendall-Roberts (JKR) model—predict spherical particles to stick to each other at small collision velocities v; above the bouncing velocity, v_b, they bounce. We study the details of the bouncing threshold using molecular dynamics simulation for crystalline nanoparticles where atoms interact via the Lennard-Jones potential. We show that the bouncing velocity strongly depends on the nanoparticle orientation during collision; for some orientations, nanoparticles stick at all velocities. The dependence of bouncing on orientation is caused by energy dissipation during dislocation activity. The bouncing velocity decreases with increasing nanoparticle radius in reasonable agreement with JKR theory. For orientations for which bouncing exists, nanoparticles stick again at a higher velocity, the fusion velocity, v_f, such that bouncing only occurs in a finite range of velocities—the bouncing window. The fusion velocity is rather independent of the nanoparticle radius.

DOI: 10.1103/PhysRevE.99.032904

I. INTRODUCTION

Collisions of nanoparticles (NPs) have attracted increased attention in the recent past. On the one hand, they are relevant in diverse areas stretching from aerosol science [1] to astrophysics [2]. There, dust grain and agglomerate collisions are decisive for the buildup of planetesimals and cometesimals in the protoplanetary disks surrounding young stars [3–5]. On the other hand, it remains unclear to what extent available macroscopic models of particle collisions also apply to the nanoworld. Recent simulational studies point at a more complex role of attractive interactions in nanocollisions than are incorporated in existing macromodels [6,7].

A basic characteristic of particle collisions is the threshold between sticking and bouncing collisions. The corresponding velocity has been termed the bouncing velocity, v_b. In a macroscopic view—such as, for instance, that expressed in the Johnson-Kendall-Roberts (JKR) model [8]—low-velocity collisions are sticking, since the elastic energy of the rebound is not sufficient to surpass the surface adhesion of the two grains; only beyond v_b, bouncing is possible.

In recent years, molecular dynamics (MD) simulations have allowed us to gain more insight into the collision characteristics of NPs. For some materials, such as silica and water ice, strong deviations from the JKR model [8] have been found [6,7]. In silica, the rupture of the neck forming between the two NPs during the outgoing collision trajectory demands more time and more work than predicted by the macroscopic model. In water ice, collision-induced heating may melt the two grains in the vicinity of the contact area; the increased NP plasticity lead to a strong increase of the bouncing velocity.

These results show that material-dependent aspects may strongly influence the collision dynamics of NPs. In this paper we want to address the question to what extent a generic material obeys the predictions of the macroscopic collision laws in the nanoworld. To this end, we study a Lennard-Jones (LJ) material. We note that this (computationally) important system has already been used repeatedly in previous work for studying NP collisions [9–16]. However, some of these simulations have been performed at higher collision energies (leading to NP fragmentation), or with strongly modified potentials, which strongly alter the collision dynamics. Thus, the bouncing behavior of pure LJ NPs needs investigation. Tanaka *et al.* [12] address this issue; however, results were only reported for a single NP radius.

MD simulations also demonstrate that at high velocities, where collisions lead to strong NP deformation, particles stop bouncing and fuse again. This is caused by the energy dissipation during the strongly inelastic collision. As a consequence, a "bouncing window" exists between the (lower) bouncing velocity, v_b, and the (higher) fusion velocity, v_f. Towards small particle radii, the bouncing window may close altogether such that collisions at all velocities are sticking.

Such considerations show that the mechanisms of energy dissipation are crucial for an understanding of NP collisions and their connection to macroscopic laws. Millán *et al.* [17,18] studied the emergence of plasticity in LJ NP collisions and showed the existence of a threshold velocity v_{ep} beyond which dislocations are formed in the colliding NPs. Its size is of a similar magnitude as the bouncing velocity. Also Takato *et al.* [15] discuss NP collisions, albeit using modified LJ potentials. They find the bouncing velocity to be in good agreement with the JKR prediction for NP radii in the range of a few nanometers. In addition they find that plasticity plays an important role in particular in the temperature dependence of

*urbassek@rhrk.uni-kl.de; http://www.physik.uni-kl.de/urbassek/

TABLE I. NP radii, R, in LJ units and numbers of atoms per NP, N, used in this study.

R	N
44.1	390 045
58.8	924 597
70.0	1 560 282
88.2	3 120 234
132.3	10 531 010

the coefficient of restitution. Later Schöner and Pöschel [19] studied Ag particles colliding with an adhesive rigid wall by MD simulations and discussed the role of dislocations and plastic slip on the coefficient of restitution.

In the present paper, we study the bouncing of NPs subject to the unmodified LJ potential; this allows us to obtain generic properties of NP collisions that can be compared to the predictions of the macroscopic JKR model. By covering a suitably wide range of NP radii, we can investigate the limits of the macroscopic JKR model. Dislocation emission is identified as the prime channel for energy dissipation, and its dependence on NP orientation is studied.

II. METHOD

We use the standard Lennard-Jones (LJ) potential with length parameter σ and energy parameter ϵ; the potential is cut off at $r_c = 5\sigma$. In the following we use LJ units which are built in the standard way from σ, ϵ, and the atom mass m. The unit of time is $\tau = \sigma\sqrt{m/\epsilon}$; lengths are measured in units of σ, and the unit of velocity is $\sqrt{\epsilon/m}$.

We build spherical NPs by cutting a sphere of radius R out of a block of fcc LJ material; the NP is then relaxed to vanishing pressure and temperature. The use of single-crystalline particles with spherical shape is the standard in atomistic simulations of NP collisions [9–19]. Even though experiments with such systems do not appear to have been reported, submicrometer-sized single-crystalline NPs are routinely used in experiments, e.g., of nanoplasticity [20–22]. Table I gives an overview of the NP radii and atom numbers used in our study.

Before starting a collision, we duplicate the NP. In the simplest case both NPs face each other with a (100) facet. To investigate the orientation dependence, one or both of the NPs are rotated before the collision, as described in detail in the next sections. All collisions are central, i.e., with a zero impact parameter; we denote the relative velocity of the grains by v. The simulations are run up to time 350 in LJ units.

After the collision, we calculate the relative center-of-mass velocity, v', of the two grains. The coefficient of restitution (COR) is then defined as

$$e = |v'|/v. \tag{1}$$

Sticking collisions obey $e = 0$.

The lowest velocity at which bouncing occurs is denoted as the bouncing velocity, v_b. We verify the difference between sticking and bouncing collisions by monitoring the time dependence of the NP trajectories. If their distance remains constant after the collision (apart from oscillations), it is a sticking collision; otherwise it is bouncing. We emphasize that in the velocity regime studied in this paper, all collisions are either bouncing or sticking. However, at higher collision velocities, other alternatives can occur, viz., fragmentation events.

The molecular dynamics simulations are performed with the LAMMPS code [23]. Atomic snapshots are generated with OVITO [24].

III. RESULTS

A. Two representative cases

In Fig. 1(a), we plot the COR for two NP orientations which exhibit drastically different behaviors. While NP 1 always collides with a (100) facet head-on, NP2 has either the same (100) orientation or collides with a heading (110) face. In the first case, the COR is zero at all velocities; in other words the two spheres stick. In the second case, we observe a bouncing window between $v = 0.02$ and 0.2. The striking distinction between these two cases is the topic of this paper and is explained in detail in Sec. III B.

We can compare this behavior with the prediction of JKR theory. COR in JKR theory has been modeled by the following law [25]:

$$e_{\mathrm{JKR}}(v) = a\sqrt{1 - \left(\frac{v_b}{v}\right)^2}. \tag{2}$$

In the original formulation, a has been set equal to 1; this amounts to ignoring all energy dissipation above the bouncing velocity. We included the factor a to allow for dissipative effects as they are the subject of this paper.

Figure 1(a) shows that—in the velocity range of $v \leqslant 0.04$—we get good agreement for the bouncing (100)(110) orientation with $v_b = 0.023$ and $a = 0.97$. Thus JKR can describe the onset of bouncing at small velocities correctly, but not the decrease of the COR at velocities >0.04 and the entire disappearance of bouncing at $v > 0.2$.

To understand the difference between the two orientations, we plot in Fig. 1(b) the fraction of defective atoms generated by the collision, at the end of the simulation. Defective atoms are non-fcc atoms as identified by common neighbor analysis with adaptative cutoff as implemented in OVITO [24]. The initial value of around 3.5% is due to surface atoms which are counted as defects. For both orientations, (almost) no defects are created at low velocities, $v \leqslant 0.04$; thereafter defect production starts and increases approximately linearly with velocity. Note that defect production is somewhat more pronounced for the nonbouncing (100)(100) case.

The defects formed are dislocations. They are generated in the contact zone where the pressure is highest, and then spread throughout the spherical grains until they are absorbed at the opposite grain surfaces, leaving behind behind planar defects [18]. These planar defects are predominantly stacking-fault planes and twin boundaries. Figure 2 shows the defective planes left behind after the collision. At low velocity, $v = 0.03$, dislocations are only generated in the nonbouncing (100)(100) case. The dislocations are embryonic and cannot leave the contact area; still their generation requires energy which then prevents the NPs from separating again. Note

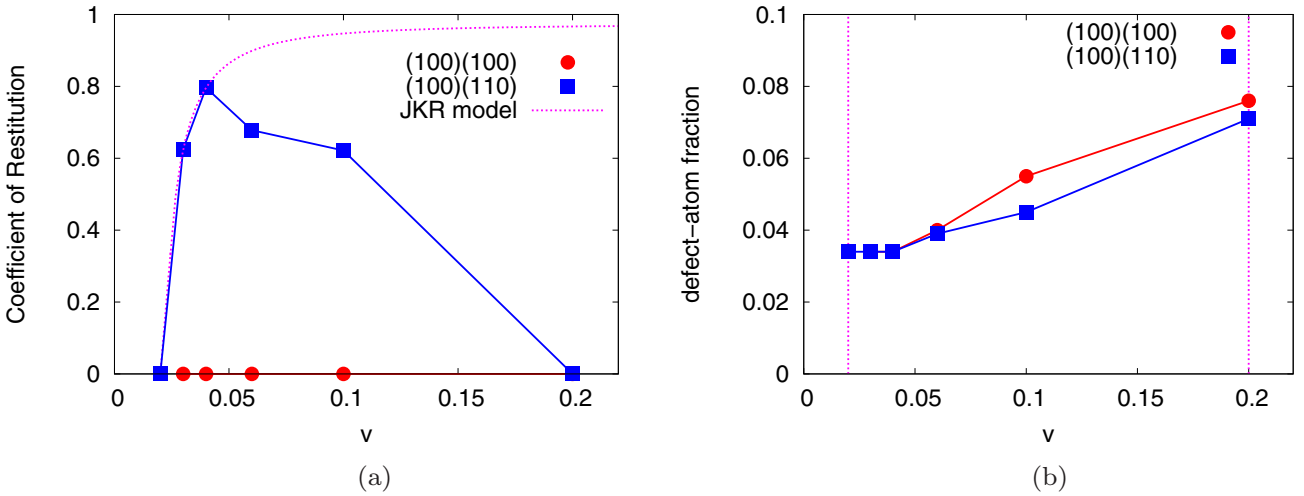

FIG. 1. Sticking (100)(100) and bouncing (100)(110) collisions for NPs of radius $R = 88.2$ as a function of collision velocity v. (a) COR as a function of velocity compared to the JKR model. (b) Fraction of defective atoms (non-fcc) generated by the collision, at the end of the simulation, as determined by CNA detection in OVITO [24]. Vertical dashed lines indicate the bouncing window for (100)(110) collisions.

that at this velocity, the (100)(110) case does not generate dislocations, but is bouncing.

At higher velocity, $v = 0.06$, also the bouncing case develops dislocations, but only in the (100)-oriented sphere. Dislocations in the (110)-oriented sphere are only generated at considerably higher velocity, $v = 0.2$; at this velocity the bouncing window ends [cf. Fig. 1(a)].

Note that the defects generated are predominantly stacking-fault planes; however, in a few cases—such as the back plane in the case of the $v = 0.1$ (100)(110) collision—twin boundaries have formed.

Figure 3 provides a zoom into the collision zone of the sticking (100)(100) collision at velocity $v = 0.1$. In addition to the stacking-fault planes spanning the entire NPs, several dislocations remained in the collision zone. Since in fcc crystals several distinct types of dislocations can exist, we analyzed their Burgers vectors. The majority of dislocations found in Fig. 3 are so-called Shockley partials, that is, dislocations with a Burgers vector of $1/6\langle 112\rangle$; these are indeed the dislocations found most commonly in fcc crystals [26]. In addition, the generation of stair-rod dislocations is notable; these are immobile [26] and hence cannot leave the collision zone. They are produced by the interaction of moving dislocations; their appearance is reminiscent of the work-hardening mechanism in heavily worked metals [26].

In fcc crystals, the dislocation glide planes are $\{111\}$ planes, on which dislocations glide in $\langle 110\rangle$ directions [27]. These planes run obliquely to the impact velocity vector for the nonbouncing (100)(100) case, as is clearly seen in Fig. 2. Note that different glide-plane orientations within the $\{111\}$ family can be activated. The activation of dislocation glide can be quantified by the Schmid orientation factor, which determines the shear stress resolved into the glide plane [26]; it is determined by the cosine of the angle between the applied stress and the glide-plane normal, multiplied by the cosine of the angle between the applied stress and the glide direction. In our simulations, the applied-stress direction is taken as the impact-velocity direction. In the bouncing case, dislocations

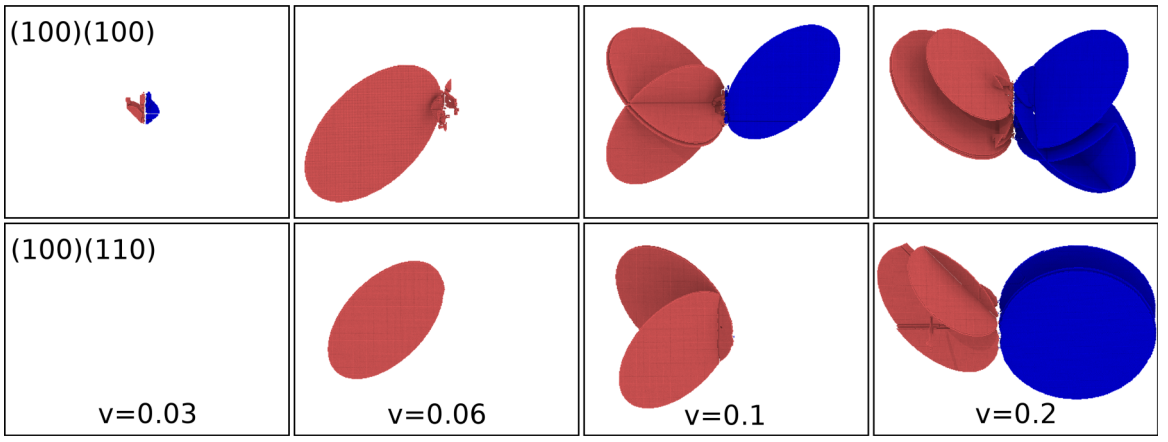

FIG. 2. Snapshots showing the dislocations and planar defects generated. Top row: Sticking (100)(100) collision. Bottom row: Bouncing (100)(110) collision. Velocities increase from left to right: $v = 0.03$, 0.06, 0.10, and 0.20. The left-hand-side NP (red or light gray) is always in (100) orientation.

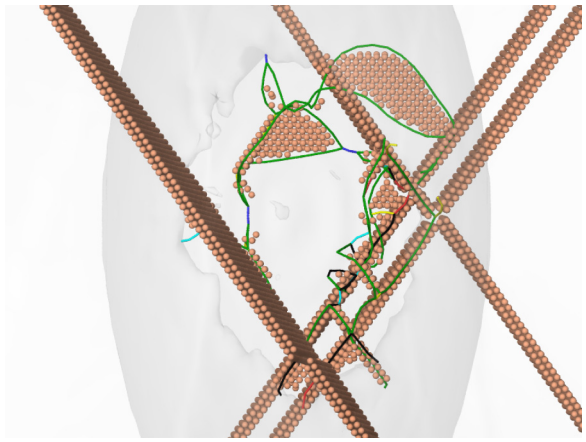

FIG. 3. Zoom-in into the collision zone of the sticking (100)(100) collision at velocity $v = 0.1$ [cf. Fig. 2(b)]. Besides the stacking-fault planes left behind by partial dislocations that swept through the grains, dislocations are left over close to the collision zone. Dislocations are colored according to their Burgers vector $\boldsymbol{b}$. Green (medium gray): Shockley partials $\frac{1}{6}\langle 112\rangle$; black: stair-rod $\frac{1}{6}\langle 110\rangle$; blue (light gray): perfect $\frac{1}{2}\langle 110\rangle$; red (dark gray): other.

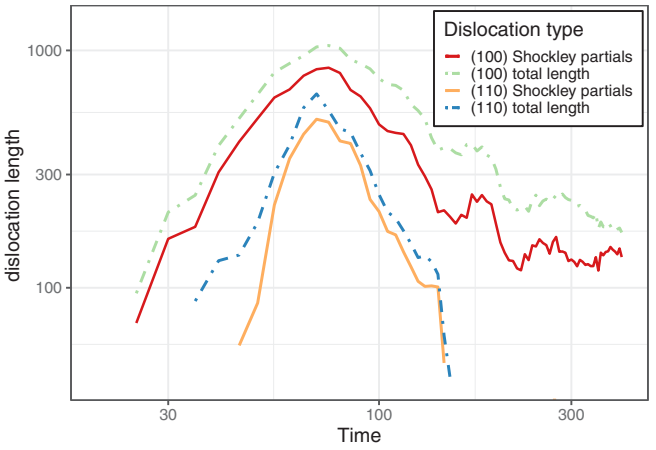

FIG. 4. Time evolution of the dislocation length in the sticking (100)(100) collision, denoted as (100), and the bouncing (100)(110) collision, denoted as (110), at a velocity of $v = 0.1$.

could travel straight on along the impact velocity in the (110) grain; however, the glide plane is now oriented perpendicular to the acting force; hence the Schmid orientation factor is zero and the glide activation is small.

From studies of nanoindentation of fcc surfaces it is known that dislocations form in the regions of the highest resolved $\{111\}\langle 110\rangle$ shear stress [28]. For example Ziegenhain *et al.* [29] have shown that the pressure necessary for nucleation of dislocations is largest for (111) and (110) surfaces and smallest for the (100) surface. This finding is in agreement with the early nucleation of plasticity found in our simulations for (100)-oriented NPs and the induced sticking. We note that in our simulations, we also find (100)(111) collisions to be entirely sticking (see Sec. III C below), in agreement with this argument.

We conclude the following from this comparison of bouncing and nonbouncing orientations.

(i) Local crystal orientations are decisive for the dislocation generation; this has already been shown previously [18].

(ii) Surface orientations, in which dislocation emission is facilitated, suffer higher energy losses and hence lead to sticking collisions; in the case shown here, bouncing is precluded altogether.

(iii) Finally, since generation of plasticity stores collision energy as potential energy inside the NPs, the COR is reduced and may vanish altogether at high dislocation generation, resulting in a finite bouncing window. This is in strict contrast to JKR theory.

B. Time evolution of dislocations

In Fig. 4 we provide the time evolution of the length of dislocation lines generated in the two collision cases studied in Sec. III A. The total length of dislocation lines shows a strong time dependence: After collision, dislocations are produced such that their lengths reach a maximum at a time of around 70. Afterwards they decay, since they are annihilated at the grain surface after they traveled through the grain leaving behind stacking-fault planes. The Shockley partials that form the most common type of dislocations in fcc crystals [26] also form the majority of dislocations found in the NP collisions analyzed here (Fig. 4).

In agreement with the snapshots of Fig. 2 displaying the final state, more dislocations are created in the sticking (100)(100) collision. The dislocations remaining in the (100)(100) collision case are found in the collision area, in the region where stacking-fault planes intersect, creating sessile junctions (see Fig. 3). In the bouncing (100)(110) case, fewer dislocations are produced, and they only exist over a small amount of time. They disappear at time $t = 150$. The amount of dislocations in this case is not large enough to lead to junctions, and this is why they disappear completely, unlike what happens in the (100)(100) case.

These data allow us to discuss the energy dissipated during the motion of dislocations. It is well known that the density of dislocations ρ moving with velocity v_d is connected to the dissipated energy via

$$E_{\text{diss}} = C \int \rho(t) v_d \, dt, \tag{3}$$

where C is a proportionality constant [30–32]. For a qualitative discussion, we may assume that v_d is constant for the same impact velocity, and the dissipated energy is hence proportional to the area under the dislocation length curves in Fig. 4.

In the bouncing (100)(110) case, fewer partials are produced, and they only exist over a small amount of time, between 40 and 200 time units. In the sticking (100)(100) case the density is much larger and the time window over which dislocations are available is larger; we conclude that energy dissipation is significantly higher in this case. This analysis is in line with the observation that this collision is sticking.

We conclude that the emission and motion of dislocations leads to energy dissipation for the (100)(100) collision larger than that for the (100)(110) collision; this explains why the former collision is sticking and the latter one is not.

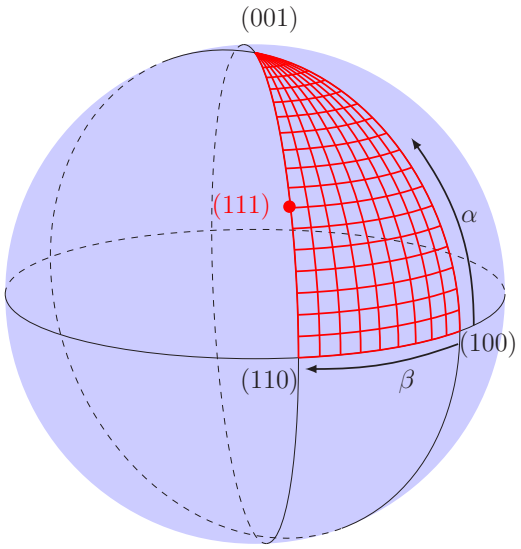

FIG. 5. Schematic view of the orientation of NP 2, defining the angles α and β. The grid line spacing is 5°.

C. Orientation dependence

In a first step, rather than randomizing completely the orientations of the two colliding NPs, we keep the orientation of NP 1 fixed such that it collides with a (100) facet head-on. NP 2 is rotated with respect to NP 1 as shown in Fig. 5; here the orientation angles α and β are introduced.

Figure 6(a) shows us the orientation dependence of the COR for a variety of collision velocities when turning NP 2 from its (100) orientation towards the (110) orientation, which will be reached at $\beta = 45°$. For velocities $v < 0.02$ and larger than $v \geqslant 0.3$, the collisions are sticking for all orientations. When rotating NP 2 from the sticking (100) direction towards the bouncing (110) direction, the COR monotonically increases. This can be understood from the arguments given in Sec. III A above, in that the activation of dislocation glide becomes increasingly difficult when NP 2 approaches the (110) direction.

In Fig. 6(b), the orientation of NP 2 varies between the bouncing (110) direction, $\alpha = 0°$, to the sticking (100) direction, $\alpha = 90°$, via another trajectory which also covers the (111) orientation, $\alpha = 35.3°$. We observe that the (111) facet is also sticking. The physics of this sticking case parallels that of the (100)(100) collision described in detail above: dislocations are produced abundantly during the collision; their generation and migration dissipate collision energy such that the NPs cannot separate after the collision. At $\alpha = 90°$, NP 2 is hit on a (001) facet (see Fig. 2); however, it is rotated by 45° with respect to the (100) facet of NP 1; this explains the high bouncing probability encountered for this orientation.

We conclude that the bouncing window closes in those orientations where dislocation emission—and hence energy dissipation—is crystallographically possible. For orientation in between these sticking directions, bouncing becomes possible.

D. Orientation average

Finally we want to obtain an overview of the NP collisions for random NP orientation. To this end, we display the averages over ten simulations, in which both NPs have average orientations, in Fig. 7. We observe that small NPs always tend to stick, while bouncing becomes more pronounced for larger NPs. This can be understood in terms of energy dissipation by dislocation generation and motion. Since the resulting defects are planar (see Fig. 2), the energy stored in these defects scales as R^2, while the total collision energy scales with R^3 for constant velocity. As a consequence, energy dissipation in dislocation generation and glide loses importance for larger NPs. Already for $R = 44$, the COR is below 10%; we did not observe any bouncing for radius $R = 29.4$, the smallest radius in our simulations.

The COR decreases with velocity towards the upper bouncing velocity. From macroscopic contact theory, it has been argued that the decay is $\propto v^{-1/4}$ [25,33,34]. In earlier MD studies of NP collisions based on modified LJ potentials, a dependence $\propto v^{-1}$ was found [14,15,35]. These authors argue that the energy dissipation caused by extensive plastic

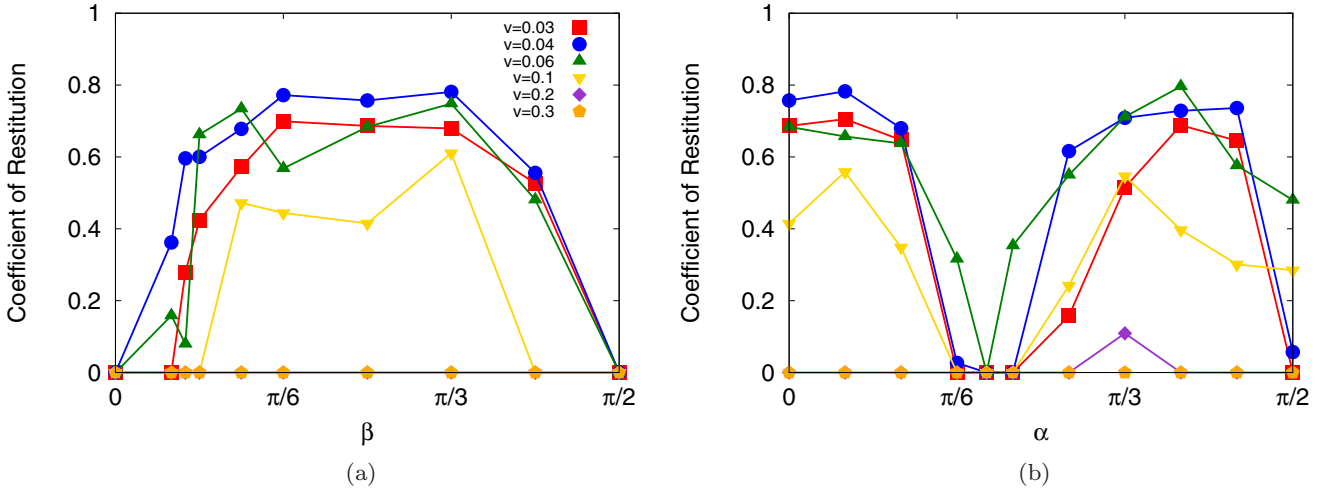

FIG. 6. COR as a function of the orientation of NP 2. (a) $\alpha = 0°$, while β is varied; (b) $\beta = 45°$, while α is varied. NP 1 always collides with a leading (100) facet. The sphere radius has been fixed to $R = 88.2$.

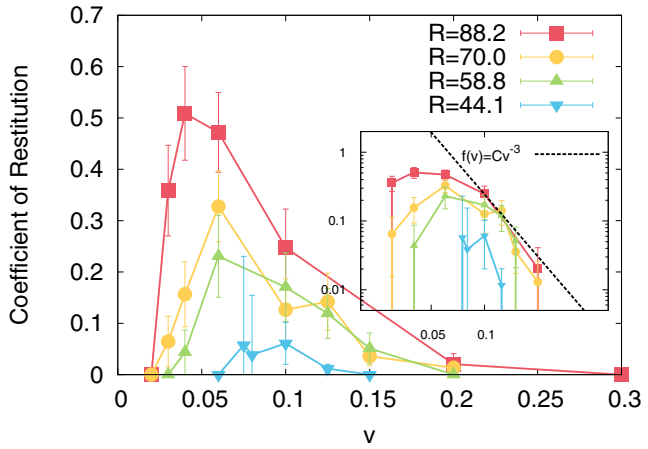

FIG. 7. COR as a function of velocity for random NP orientations and various radii R; the inset demonstrates a decay $\propto v^{-3}$ at large velocities. Error bars denote the standard deviation of an ensemble of ten simulations.

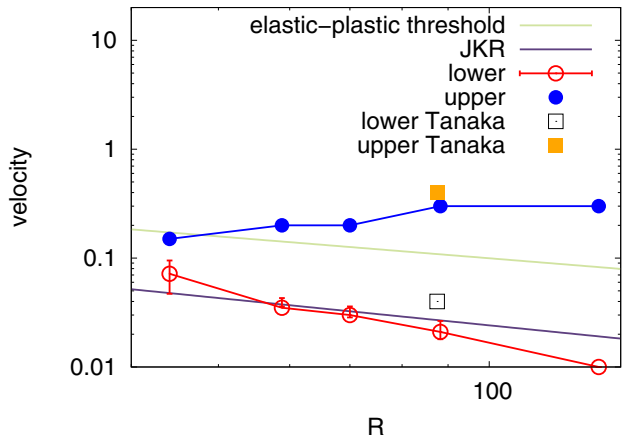

FIG. 8. Dependence of the upper bouncing velocity, v_b, and the lower bouncing velocity, v_f, on the NP radius R. Comparison to the data by Tanaka *et al.* [12, Fig. 7], $R = 87.6$, to JKR theory, Eq. (5), and to the elastic-plastic threshold, Eq. (6). Data are averages over ten random orientations, with the exception of the data for $R = 132$, which is based on a single simulation.

deformation, which is observed in the simulation but not sufficiently included in the macroscopic theory, causes the stronger falloff of the COR. We find here from the data shown in Fig. 7 a stronger decay, approximately proportional to v^{-3}, for velocities above $v = 0.1$. It may be surmised that this even stronger falloff of the COR is caused by our consequent use of the LJ potential for all atoms. The previous studies [14,15,35] used potentials that artificially enhance the bouncing probability by reducing the interparticle attraction or even using purely repulsive potentials between atoms of different NPs. In our case, the bouncing probability is reduced by the stronger interparticle adhesion warranted by the unmodified LJ interaction, leading to higher energy dissipation and a consequently stronger decay of the COR with velocity.

As a second feature, we observe that the bouncing window has an upper limit, v_f, which is rather constant at $v_f = 0.3$. At these large velocities, already strong deformations of the NP at the surface can be seen which mostly originate from slip and which lead to high energy dissipation and to NP fusion [18].

In Fig. 8, we plot the upper and lower velocities of the bouncing window as observed in our simulations. The lower bouncing velocities are obtained from a fit of the COR data in Fig. 7 to the JKR estimate, Eq. (2). Note that for the largest sphere, $R = 132$, we simulated only a single orientation so that this data point may not be representative. In this logarithmic presentation the decrease of the lower bouncing velocity v_b can be seen more clearly. We compare with the literature data of Tanaka *et al.* [12], who simulated the collision of $R = 87.6$ NPs similar to what we have done. We evaluate the bouncing window boundaries from their Fig. 7; they are in reasonable agreement with our results.

We can compare our simulation results for the bouncing velocity v_b with the prediction of JKR. The JKR model predicts the bouncing velocity of two identical NPs of radius R to be determined by the surface energy γ, the indentation modulus $E_{\rm ind}$, and the mass density ρ via [25,36,37]

$$v_b = \left(\frac{C}{\rho}\right)^{1/2}\left(\frac{\gamma^5}{E_{\rm ind}^2 R^5}\right)^{1/6}. \tag{4}$$

Here, C is a constant which—depending on the model assumptions—assumes values between 0.30 and 18.3 [25,36–38]. Using values appropriate for a LJ material—$\gamma = 2.3$, $E_{\rm ind} = 107$, and $\rho = 1.085$ [17]—Eq. (4) simplifies to

$$v_{\rm JKR} = C^{1/2}\frac{0.405}{R^{5/6}}. \tag{5}$$

Figure 8 compares the prediction, Eq. (5), to our simulation results. The bouncing velocity was calculated as an average over the bouncing collisions only. A least-square fit yields $C = 7.66$; this value is well within the range of $C = 0.3, \ldots, 18.3$ discussed in the literature [25,36–38]. Note that for the largest sphere, $R = 132$, we have no statistics since our data are based on a single bouncing collision; the bouncing velocity of the other four radii are within the error bars described by Eq. (5).

Finally, we relate our data with the onset of plasticity that has recently been obtained by an extensive series of simulations of LJ NP collisions; it is located at [17,39]

$$v_{\rm ep} = \frac{2.15}{R^{2/3}}. \tag{6}$$

Figure 8 shows that the onset of plasticity is located (slightly) above the bouncing velocity. This is in agreement with our finding [Fig. 1(b)] that dislocations are only generated above the bouncing velocity. As the power exponents in Eqs. (5) and (6) indicate, and as is confirmed by Fig. 8, the velocity range above the bouncing velocity in which the collision is purely elastic widens for larger NPs. Millán *et al.* [17] find that for NP radii of $R = 15$, collisions produce no dislocations up to collision velocities of $v = 0.3$, i.e., at the fusion velocity. Since we find the bouncing velocity to be below the elastic-plastic threshold, this is in agreement with our finding that at such low velocities bouncing has ceased.

IV. SUMMARY

From our MD simulations of LJ NP collisions we can draw the following conclusions.

(i) At small radii $R \lesssim 30$ no bouncing is observed. NPs stick to each other since adhesive forces gain importance for small radii.

(ii) At radii larger than around 30, a bouncing window opens up. The bouncing velocity, v_b, is in reasonable agreement with the JKR prediction.

(iii) Towards high velocities, the fusion velocity, v_f, separates the bouncing regime from the fusion of strongly deformed NPs. The fusion velocity is approximately independent of NP size at $v_f = 0.3$.

(iv) Generation of dislocations sets in at the elastic-plastic threshold, v_{ep}, which is slightly larger than the bouncing velocity.

(v) The generation of dislocations is strongly dependent on the NP orientation. Orientations which allow for easy dislocation generation are found to be sticking at all velocities, since the energy that would be necessary for NP separation is dissipated during the collision.

(vi) The COR shows at small velocities the characteristic rise predicted by the JKR model above the bouncing velocity. This characterizes a regime where no dislocations are generated. The COR never reaches the value of 1, since all collisions are inelastic; neck formation and, at higher velocities, dislocation generation and eventually strong NP deformation dissipate energy. At higher velocities, however, the COR decays again and reaches zero at the fusion velocity.

In the present study, we focused on ideal single-crystalline NPs. In the future it might be interesting to investigate the influence of preexisting defects in the colliding NPs. In reality, NPs may be polycrystalline and contain defects such as point defects, dislocations, and twins from previous collisions; thus their microstructure may deviate considerably from the ideal single-crystalline setup considered here. The stress required to to move preexisting dislocations would be significantly lower than the stress required to nucleate new dislocations [26]. The stress required to induce grain boundary activity in polycrystals is also much lower than the dislocation nucleation stress [40]. Therefore, threshold velocities for plastic energy dissipation could be significantly lower than those in the perfect crystal case. For amorphous nanoparticles, the formation of shear transformation zones [41] would provide an effective energy dissipation channel. We note that we performed a series of exploratory simulations for amorphous NPs; however, in the size range investigated here, all collisions were sticking and no bouncing was found.

A further issue to be studied is the relevance of other energy dissipation channels such as the excitation of NP oscillations. Here it should be noted that macroscopic models of NP collisions including NP oscillations predict a strong influence of these oscillations on the COR if the duration of particle contact equals the NP oscillation period [42,43]. It will be interesting to study the influence of such oscillations on the bouncing behavior.

ACKNOWLEDGMENTS

We acknowledge financial support by the Deutsche Forschungsgemeinschaft within Project No. Ur 32/27-2. E.M.B. thanks support from Grant No. PICT2014-0696. Simulations were performed at the High Performance Cluster Elwetritsch (RHRK, TU Kaiserslautern, Germany).

[1] M.-Y. Yi, D.-S. Kim, J.-W. Lee, and J. Koplik, Aerosol Sci. **36**, 1427 (2005).
[2] J. Blum, Res. Astron. Astrophys. **10**, 1199 (2010).
[3] T. Birnstiel, M. Fang, and A. Johansen, Space Sci. Rev. **205**, 41 (2016).
[4] M. S. Bentley, R. Schmied, T. Mannel, K. Torkar, H. Jeszenszky, J. Romstedt, A.-C. Levasseur-Regourd, I. Weber, E. K. Jessberger, P. Ehrenfreund *et al.*, Nature (London) **537**, 73 (2016).
[5] Y. Langevin, M. Hilchenbach, N. Ligier, S. Merouane, K. Hornung, C. Engrand, R. Schulz, J. Kissel, J. Rynö, and P. Eng, Icarus **271**, 76 (2016).
[6] M. L. Nietiadi, P. Umstätter, T. Tjong, Y. Rosandi, E. N. Millán, E. M. Bringa, and H. M. Urbassek, Phys. Chem. Chem. Phys. **19**, 16555 (2017).
[7] M. L. Nietiadi, P. Umstätter, I. Alabd Alhafez, Y. Rosandi, E. M. Bringa, and H. M. Urbassek, Geophys. Res. Lett. **44**, 10,822 (2017).
[8] K. L. Johnson, K. Kendall, and A. D. Roberts, Proc. R. Soc. London, Ser. A **324**, 301 (1971).
[9] M. Kalweit and D. Drikakis, Phys. Rev. B **74**, 235415 (2006).
[10] H. Kuninaka and H. Hayakawa, Phys. Rev. E **79**, 031309 (2009).
[11] K. Saitoh, A. Bodrova, H. Hayakawa, and N. V. Brilliantov, Phys. Rev. Lett. **105**, 238001 (2010).
[12] H. Tanaka, K. Wada, T. Suyama, and S. Okuzumi, Prog. Theor. Phys. Suppl. **195**, 101 (2012).
[13] S.-C. Jung, J.-G. Bang, and W.-s. Yoon, J. Aerosol Sci. **50**, 26 (2012).
[14] Y. Takato, S. Sen, and J. B. Lechman, Phys. Rev. E **89**, 033308 (2014).
[15] Y. Takato, M. E. Benson, and S. Sen, Phys. Rev. E **92**, 032403 (2015).
[16] Y. Takato, M. E. Benson, and S. Sen, Proc. R. Soc., Ser. A **474**, 20170723 (2018).
[17] E. N. Millán, D. R. Tramontina, H. M. Urbassek, and E. M. Bringa, Phys. Chem. Chem. Phys. **18**, 3423 (2016).
[18] E. N. Millán, D. R. Tramontina, H. M. Urbassek, and E. M. Bringa, Phys. Rev. E **93**, 063004 (2016).
[19] C. Schöner and T. Pöschel, Phys. Rev. E **98**, 022902 (2018).
[20] J. R. Greer, C. R. Weinberger, and W. Cai, Mater. Sci. Eng., A **493**, 21 (2008).
[21] D. Mordehai, M. Kazakevich, D. J. Srolovitz, and E. Rabkin, Acta Mater. **59**, 2309 (2011).
[22] D. Mordehai, S.-W. Lee, B. Backes, D. J. Srolovitz, W. D. Nix, and E. Rabkin, Acta Mater. **59**, 5202 (2011).

[23] S. Plimpton, J. Comput. Phys. **117**, 1 (1995), http://lammps.sandia.gov/.
[24] A. Stukowski, Modell. Simul. Mater. Sci. Eng. **18**, 015012 (2010), http://www.ovito.org/.
[25] S. Krijt, C. Güttler, D. Heißelmann, C. Dominik, and A. G. G. M. Tielens, J. Phys. D **46**, 435303 (2013).
[26] D. Hull and D. J. Bacon, *Introduction to Dislocations*, 5th ed. (Butterworth-Heinemann, Kidlington, UK, 2011).
[27] It is standard crystallographic notation to denote lattice planes by round brackets, such as (100), and directions by square brackets, such as [100]. Families of crystallographically equivalent planes are denoted by curly brackets, such as {100}, and families of crystallographically equivalent directions by angled brackets, such as ⟨100⟩.
[28] C. J. Ruestes, E. M. Bringa, Y. Gao, and H. M. Urbassek, in *Applied Nanoindentation in Advanced Materials*, edited by A. Tiwari and S. Natarajan (Wiley, Chichester, UK, 2017), Chap. 14, pp. 313–345.
[29] G. Ziegenhain, H. M. Urbassek, and A. Hartmaier, J. Appl. Phys. **107**, 061807 (2010).
[30] H. Quinney and G. I. Taylor, Proc. R. Soc. London A **163**, 157 (1937).
[31] A. Higginbotham, E. M. Bringa, J. Marian, N. Park, M. Suggit, and J. S. Wark, J. Appl. Phys. **109**, 063530 (2011).
[32] J. F. Rodriguez-Nieva, C. J. Ruestes, Y. Tang, and E. M. Bringa, Acta Mater. **80**, 67 (2014).
[33] K. L. Johnson, *Contact Mechanics* (Cambridge University, Cambridge, UK, 1985).
[34] G. Weir and P. McGavin, Proc. R. Soc. London, Ser. A **464**, 1295 (2008).
[35] A. I. Ayesh, S. A. Brown, A. Awasthi, S. C. Hendy, P. Y. Convers, and K. Nichol, Phys. Rev. B **81**, 195422 (2010).
[36] C. Thornton and Z. Ning, Powder Technol. **99**, 154 (1998).
[37] N. V. Brilliantov, N. Albers, F. Spahn, and T. Pöschel, Phys. Rev. E **76**, 051302 (2007).
[38] C. Dominik and A. G. G. M. Tielens, Astrophys. J. **480**, 647 (1997).
[39] The equation for the bouncing velocity in Ref. [18] was misprinted; The equation in Ref. [17] is correct.
[40] M. A. Meyers, A. Mishra, and D. J. Benson, Prog. Mater. Sci. **51**, 427 (2006).
[41] T. C. Hufnagel, C. A. Schuh, and M. L. Falk, Acta Mater. **109**, 375 (2016).
[42] R. Murakami and H. Hayakawa, Phys. Rev. E **89**, 012205 (2014).
[43] W. C. Tucker, A. R. Dove, and P. K. Schelling, Comput. Mater. Sci. **161**, 215 (2019).